Available online at www.sciencedirect.com
ScienceDirect
Scripta Materialia 56 (2007) 733–736
Scripta MATERIALIA
www.actamat-journals.com

Aluminum element effect for electron beam welding of similar and dissimilar magnesium–aluminum–zinc alloys

Chao-Ting Chi,[a,b,*] Chuen-Guang Chao,[a] Tzeng-Feng Liu[a] and Chuan-Hua Lee[b]

[a] *Department of Materials Science and Engineering, National Chiao Tung University, Hsinchu 300, Taiwan, ROC*
[b] *System Manufacturing Center, Chung-Shan Institute of Science and Technology, P.O. Box 90008-14, Sanxia 237, Taipei, Taiwan, ROC*

Received 20 December 2006; revised 16 January 2007; accepted 17 January 2007
Available online 20 February 2007

Defects causing stress concentration from electron beam welding are related to the Al content of the Mg–Al–Zn weldment and its effect will be most conspicuous for the welding of dissimilar metals. Precipitates which are γ phase ($Mg_{17}(Al,Zn)_{12}$) also influence the formative mechanism of pores, the heat-affected zone and the fracture mode of the weld. More noteworthy is that the Al content of 6.0 wt.% is a very important delimitation for these mechanisms.

Keywords: Aluminum; Electron beam welding; Magnesium alloys; Precipitation

Given environmental protection concerns, magnesium alloy has recently becoming one of the most important lightweight materials because of its low density, high specific strength and superior properties for absorbing vibration and insulating electromagnetic interference. Traditional welding of magnesium alloys, however, requires high power under flux, a shielding gas or a vacuum environment due to the high level of chemical activity and thermal conduction. Not only are the grains coarsened (gas tungsten arc-welding has a grain size about 50–70 μm in the fusion zone and a joint efficiency of 70–90% [1]), but many cavities and cracks form in the fusion zone or heat-affected zone (HAZ) [2,3]. The weld structure will easily recrystallize if strain hardening is performed before conventional welding [4]. Hence, the weld strength is much lower than that of the base material.

High energy beam welding can eliminate the aforementioned shortcomings with its low input energy, narrow HAZ, high welding precision and high depth-to-width ratio [5]. A fine crystal weld structure can be formed by fast cooling resulting from high thermal conduction [6], and its high Al content can produce brittle precipitates for increased weldment strength [7]. Studies on precise magnesium alloy welding to date have concentrated on laser welding [8–10] because of its convenience. However, the complete join depth of laser welding is limited [11] by optical device tolerance for beam power. On the other hand, electron beam welding (EBW) with joint efficiency above 90% [4] is advantageous for a larger penetration depth. With matched control parameters, EBW can generate energy with symmetrical Gaussian distribution to form a sound weld [12,13]. Therefore, systematic research for parameter optimization of similar metals welding (SMW) is necessary for improving the weldment quality [14]. Meanwhile, the estimated joint efficiency (how close the strength of the optimum weldment is to that of the base material) and process window (how easy it is to fabricate a high strength weldment under unknown welding conditions) [15] can be used as a reference for dissimilar metals welding (DMW).

Providing a flexible design [16] for both technical and economic considerations is possible with wide DMW use. DMW can be divided into two categories: (i) different major and minor compositions between butting materials; and (ii) the same major composition but different minor composition. Compared with SMW, DMW possesses a more complex structure, resulting from a concentration gradient in the chemical composition. Therefore, this subject deserves more than passing notice. Four recent articles have reported on the use of DMW for butting Mg and Al alloys [17–20]. In this work, DMW for butting AZ-series alloys will be studied with experiments and analysis.

Home-made AZ31B, AZ61A and AZ91D extruded plates of dimensions $105 \times 60 \times 12\ mm^3$ were used. A 0.5-mm-thick layer was removed from the surface to avoid

* Corresponding author. Address: Department of Materials Science and Engineering, National Chiao Tung University, Hsinchu 300, Taiwan, ROC; e-mail: chaoting@ms31.url.com.tw

1359-6462/$ - see front matter
doi:10.1016/j.scriptamat.2007.01.028

any native oxide effect. These work pieces were cleaned by acetone, reserved in a vacuum desiccator (1×10^{-3} Torr) and then welded together by a butting process but without filler in a work chamber under high vacuum (3×10^{-5} Torr). The EBW control parameters were optimized in previous research [21], with a 30 mA beam current, a 120 kV accelerating voltage and a 30 mm s^{-1} welding speed, with the focus position at the bottom. The resulting weldment dimensions were $105 \times 119 \times 11$ mm^3.

The weldment's tensile properties was analyzed precisely as follows. Welds at the halfway point along the gage length in standard tensile specimens were perpendicular to the longitudinal direction. These weldments were then cut into one metallographic ($15 \times 10 \times 11$ mm^3) and six tensile specimens (according to the subsize specimen in ASTM B557-02 standard inspection [22]) along the extruded direction. Three tensile specimens were milled on the surface and bottom to be used as non-stress-concentration specimens, while the other three were used without milling as specimens to study the stress-concentration influence.

Microstructure changes were analyzed using a scanning electron microscope, an energy dispersive spectrometer, a transmission electron microscope, an electron probe X-ray micro-analyzer, and a Vickers hardness testing machine. Finally, the metallographic specimens were grinded step-by-step to identify the preferred orientation and phase composition by X-ray diffraction.

The chemical compositions of the AZ31B, AZ61A and AZ91D magnesium alloys were analyzed using inductively coupled plasma-atom emission spectrometer and mass spectrometer. In Table 1, all of the chemical element contents meet ASTM standard specifications.

Figure 1(a)–(c) indicates metallographic photographs of weld cross-sections with SMW for AZ31B, AZ61A and AZ91D, respectively. They were observed to have an increasing number of pores in the fusion zone with increasing Al content. This is because the base material was exposed to 350 °C for more than 6 h in atmosphere during the extrusion processes and the preheating. Also, γ phase ($Mg_{17}Al_{12}$) and oxygen molecules were combined into MgO, Al_2O_3 or $MgAl_2O_4$ because of their high affinity [23–25]. Once these γ phase precipitates containing oxygen were melted by the high energy density of the electron beam, the oxygen emerged into micropores [21].

Figure 2 shows that the ultimate tensile strength ratio (weldment/matrix) increases with increasing Al content, regardless of which base material or stress-concentration weldment with SMW (78.9%, 82.7% and 83.7%) or DMW (49.4%, 70.2% and 74.6%) is used. The main reason is that δ phase (solid solution phase) grains contain more Al atoms by means of solid solution, and then the remnant Al will precipitate the brittle γ phase from the grain boundary. The homogeneity of the base material is damaged by these precipitates, which results in the ductility tending to decrease with increasing aluminum content. The problem increases when one turns from SMW to DMW. The DMW shows lower strength and elongation than the SMW when tested in the as-welded condition. This is due to root concavity, which is possibly the result of turbulence in the weld pool caused by regions of differing fluidity. Meanwhile, the melting alloy with higher Al content (or lower liquidus temperature) has better fluidity to fill defects with constant energy and a fast cooling weld pool. As shown in Figure 1(d)–(f), the depth of weld root concavity decreases with increasing average Al content in the weld.

Table 1. Chemical composition for AZ-series alloys (wt.%)

Materials	Element				
	Mg (Cu)	Al (Fe)	Zn (P)	Mn (Pb)	Si (Be)
AZ31B	96.2467 (0.0004)	2.8150 (0.0025)	0.6395 (0.0013)	0.2835 (0.0008)	0.0094 (0.0009)
AZ61A	93.0585 (0.0007)	5.8800 (0.0030)	0.7985 (0.0012)	0.2205 (0.0062)	0.0240 (–)
AZ91D	90.3148 (0.0012)	8.8550 (0.0041)	0.5474 (0.0012)	0.2600 (0.0017)	0.0143 (0.0003)

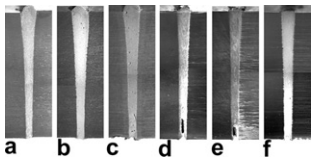

Figure 1. Comparison of cross-sections of welds with SMW: (a) AZ31B, (b) AZ61A, (c) AZ91D, and DMW: (d) AZ31B–AZ61A, (e) AZ31B–AZ91D, (f) AZ61A–AZ91D. Plate thickness is 11 mm.

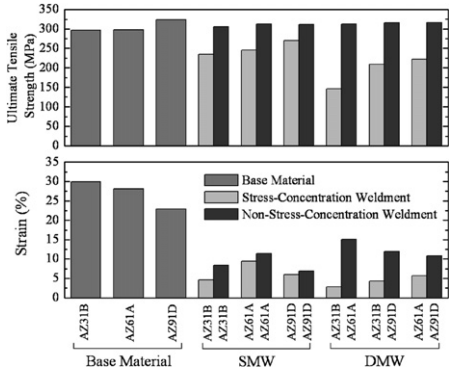

Figure 2. Pictograph of strength and strain of weldment with SMW and DMW for AZ-series alloys.

The strength of non-stress-concentration weldment increases slightly with Al content if the surface stress raiser is removed by milling, and is much stronger than stress-concentration weldment. This implies that the best quality of weldment with DMW can be obtained as with SMW. Furthermore, the strength ratio for non-stress-concentration weldment is higher than 100% for an Al content less than the average 7.5 wt.%, but is only 97.8% for 9.0 wt.% Al. This results from work hardening by milling and the larger number of pores in the weld, respectively. On the other hand, the ductility of non-stress-concentration weldment can improve with original tendency for that of base material. The weld has a cast structure, so its elongation is much lower than that of extruded material. However, the average Al content for non-stress-concentration weldments can be ranked in order of decreasing ductility as follows: 4.5, 6.0, 7.5, 3.0 and 9.0 wt.%. This is further discussed later on.

Figure 3(a)–(c) shows metallographic photographs of weld crest boundaries with DMW for sides of AZ31B, AZ61A and AZ91D, respectively. Precipitate growth

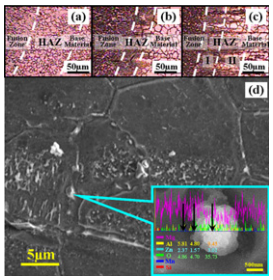

Figure 3. Metallographic photographs of weld boundary for (a) AZ31B, (b) AZ61A, (c) AZ91D, and (d) SEM photograph with EDS analysis for HAZ enlargement of AZ61A.

modes are similar to those of SMW. These precipitates concentrate in the fusion zone, in forms ranging from scattered particles to dense dendrites as the Al content increases. Compared with the weld boundary with SMW for the same base material, more particles and fewer dendrites are distributed on either side of the weld with DMW. This results from balancing the Al element, as shown in Figure 4. At low content levels, the Zn element moves simultaneously with the Al element, thus contributing to the decrease in the Gibbs free energy of precipitates [26]. Therefore, according to recent research [23], part of the Al can be replaced with Zn for $Mg_{17}Al_{12}$, indicated by $Mg_{17}(Al,Zn)_{12}$. Additionally, the high oxygen content of the precipitate also proves the possibility of pore formation, as revealed in Figure 3(d).

Figure 3(a)–(c) shows that the width of the HAZ and the precipitating state of the submicron-sized crystals (γ phase) depend on the Al content. When the Al content is 3.0 wt.%, the width of the HAZ is about 80–100 μm and its average grain size (10 μm) is greater than that of the base material (5 μm). When the Al content is increased to 6.0 wt.%, the width decreases to about 30–40 μm and its average grain size (20 μm) is still greater than that in the base material (15 μm). At this time, submicron-sized crystals are present and distributed over the inside of grains (δ phase) in the HAZ. When the aluminum content reaches 9.0 wt.%, the HAZ can be divided into two parts. One part, HAZ-I, is the partially melted zone beside the fusion zone [1], just as it was with 6.0 wt.% Al. The other part, HAZ-II, is 50–60 μm in width beside the base material without grain growth (15 μm), which only precipitates submicron-sized crystals around the grain boundary phase. If a 1.5-μm-diameter precipitate in HAZ is selected and centered on the pre-cutting area, as

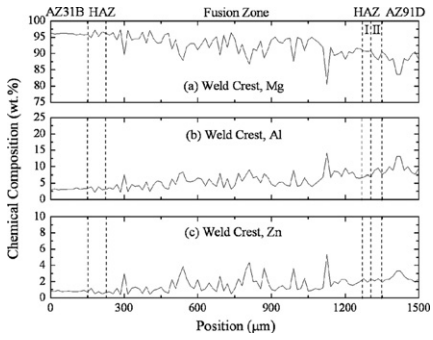

Figure 4. EPMA analysis of weld crest with DMW (AZ31B–AZ91D) for (a) Mg, (b) Al and (c) Zn.

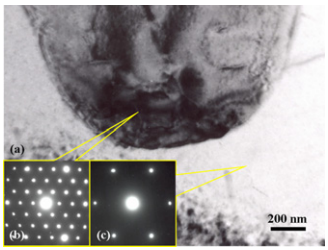

Figure 5. TEM photographs and electron diffraction pattern in HAZ for AZ61A: (a) bright field image, (b) electron diffraction pattern with $[\bar{1}\,1\,1]$ zone axis for γ phase and (c) electron diffraction pattern with [0 0 0 1] zone axis for δ phase.

shown in Figure 3(d), the specimen can be fabricated by focusing a Ga ion beam to observe the relationship between the γ and δ phases. Figure 5 shows that the precipitate of the γ phase is in a polycrystalline state (average grain size is about 0.2 μm) whose unit cell (base-centered cubic structure, $a = 10.5600$ Å, $\alpha = \beta = \gamma = 90°$) is much larger than that of the δ phase (hexagonal close-packed structure, $a = b = 3.2095$ Å, $c = 5.2104$ Å, $\alpha = \beta = 90°$, $\gamma = 120°$) in terms of its electron diffraction pattern.

When Al and Zn contents reach only 3.0 and 1.0 wt.%, respectively, the submicron-sized crystals cannot be precipitated in the grain according to the Mg–Al–Zn ternary phase diagram [27]. Therefore, the remnant energy in HAZ can only coarsen grains during EBW. Increasing the Al content often causes the γ phase to precipitate continuously along the grain boundary under slow cooling [15]. As the HAZ temperature is raised to between 610 °C (liquidus temperature) and 437 °C (eutectic temperature) again, many Al atoms diffuse quickly from the liquid-state γ phase to the solid-state δ phase via solid solution. Once the alloy is quickly cooled from the eutectic temperature to room temperature, the maximum solid solubility of Al in the precipitate vicinity decreases immediately from 11.5 to about 2.0 wt.%. Most Al atoms cannot return to the grain boundary in time, so the γ phase will nucleate and grow directly into the submicron-sized crystals by partial HAZ energy at their present positions, as shown in Figure 3(d). Therefore, the width of the narrowed grain coarsening zone of AZ61A alloy is slightly wider than the coarsening grain diameter. With regard to AZ91D weldment, its continuous γ phase, which extends further across the HAZ than the AZ61A weldment, can be melted to reform the wider distribution of submicron-sized precipitates during fast solidifying at 437 °C. The EBW for AZ61A alloy according to the foregoing viewpoints possesses optimal weldability because of the narrowest HAZ.

As shown in Figure 6(a) and (e), the $(10\bar{1}0)$ plane lying on the transverse plane of the extruded plate is the preferred orientation before EBW. The weld structure changes from forging to casting after EBW, and the original preferred orientation gradually disappears in Figure 6(c). The HAZ diffraction pattern is a transitional state between the base material and the fusion zone, as shown in Figure 6(b) and (d). The γ phase is the sole intermetallic compound, but its peak is not well marked. Because peak intensity increases with Al content in Mg alloys, it is only found in Figure 6(d) and (e) after balancing the Al element of the weld with DMW.

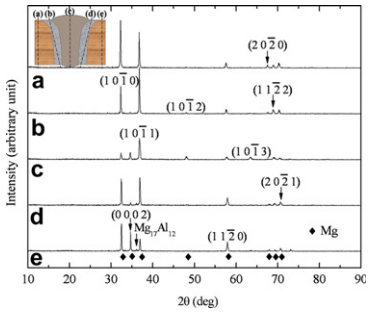

Figure 6. XRD analysis of weld with DMW for AZ31B–AZ91D: (a) base material for AZ31B, (b) HAZ beside AZ31B, (c) fusion zone, (d) HAZ beside AZ91D and (e) base material for AZ91D.

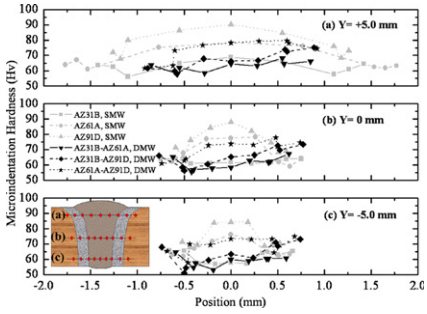

Figure 7. Vickers hardness test on weld cross-section with SMW and DMW (the left alloy with low Al content) for AZ-series alloys.

Figure 7 shows test positions and results of Vickers hardness for the cross-section of welds. No matter whether by SMW or DMW, the Vickers hardness of the fusion zone, the HAZ and the base material increases with increasing Al content. The brittle γ phases for SMW concentrate mainly in the weld crest center, causing the Vickers hardness to drop from the central line of the fusion zone to the base material and from top to bottom. The DMW precipitates concentrate mainly on the high Al content side of the weld crest, causing the Vickers hardness to reduce from right to left and from top to bottom. The vertical and horizontal test results all match the analyzed result presented in Figure 4. Moreover, a sudden decrease of Vickers hardness occurs in the HAZ as it is affected by annealing softening. The situation for DMW is particularly serious, such as $(-0.6, 5.0)$, $(-0.5, 0)$ and $(-0.5, -5.0)$, because these positions become the lowest values along the continuously descending hardness. Therefore, the weldment fracture mode for DMW belongs to the regular HAZ fracture, initiating from the weld root concavity and propagating along these positions. Two SMW fracture modes occur for AZ-series weldments: the irregular fusion zone fracture with an aluminum content below 6.0 wt.%; and the regular heat-affected zone fracture with an aluminum content above 6.0 wt.%. This is caused by many precipitates concentrating in the fusion zone, which range in form from scattered particles to dense dendrites as the aluminum content increases [15].

To conclude: first, the melted magnesium alloy with higher Al content has better fluidity to chink surface defects during electron beam welding, but the γ phase ($Mg_{17}(Al,Zn)_{12}$) containing oxygen can be dissolved and form micropores during high energy electron beam welding. Therefore, Al content, composition distribution and parameter condition are three major factors to form defects for Mg–Al–Zn weldment.

Next, the formation mechanism for the heat-affected zone of Mg–Al–Zn weldment can occur in two modes: grain coarsening and submicron-sized crystal precipitating. AZ31B exhibits the former mode, and AZ91D exhibits the latter. AZ61A, on the other hand, exhibits the two modes and forms the narrowest heat-affected zone.

Finally, the distribution of γ phase for similar and dissimilar metal welding can be formed by symmetrical distribution and gradient distribution, respectively. The former can change the fracture mode from an irregular fusion zone fracture to a regular heat-affected zone fracture with increasing Al content; the latter has only the regular heat-affected zone fracture mode due to quirky composition and property in the weld.

The authors would like to thank M.D. Que of Missile and Rocket Systems Research Division in Chung-Shan Institute of Science and Technology for technical assistance.

[1] S.F. Su, J.C. Huang, H.K. Lin, N.J. Ho, Metall. Mater. Trans. 33A (5) (2002) 1461–1473.
[2] M.M. Avedesian, H. Baker, Magnesium and Magnesium Alloys, ASM International, Materials Park, OH, 1999.
[3] Z. Sun, J. Wei, D.Y. Pan, Y.K. Tan, Sci. Technol. Weld. Joining 7 (6) (2002) 343–351.
[4] R.W. Messler, Principles of Welding, Wiley-Interscience, New York, 1999.
[5] U. Draugelates, A. Schram, B. Bouaifi, C. Kettler, Magnesium Alloys Appl. (1998) 29–35.
[6] A. Weisheit, R. Galun, Weld. J. 77 (4) (1998) 148–154.
[7] H. Haferkamp, U. Dilthey, G. Träger, I. Burmester, M. Niemeyer, Magnesium Alloys Appl. (1998) 595–600.
[8] A. Weisheit, R. Galun, B.L. Mordike, Weld. J. (1998) 149–154.
[9] L.K. Pan, C.C. Wang, Y.C. Hsiao, K.C. Ho, Opt. Laser Technol. 37 (2004) 33–42.
[10] L.K. Pan, C.C. Wang, Y.C. Shin, H.F. Sher, Sci. Technol. Weld. Joining 10 (4) (2005) 1–8.
[11] D.E. Powers, G.R. Laflamme, Weld. J. (1992) 47–52.
[12] E. Koleva, Vacuum 77 (2005) 413–421.
[13] U. Dilthey, J. Weiser, Weld. World 39 (2) (1997) 89–98.
[14] E. Koleva, I. Vuchkov, Vacuum 77 (2005) 423–428.
[15] C.T. Chi, C.G. Chao, T.F. Liu, C.C. Wang, Mater. Sci. Eng. A 435–436 (2006) 672–680.
[16] Z. Sun, R. Karppi, J. Mater. Process. Technol. 59 (1996) 257–267.
[17] K. Kato, H. Tokisue, Weld. World 18 (11) (2004) 861–867.
[18] Y.S. Sato, S.H.C. Park, M. Michiuchi, H. Kokawa, Scripta Mater. 50 (2004) 1233–1236.
[19] S. Hirano, K. Okamoto, M. Doi, H. Okamura, M. Inagaki, Y. Aono, Weld. Int. 18 (9) (2004) 702–708.
[20] J.C. Yan, Z.W. Xu, Z.Y. Li, L. Li, S.Q. Yang, Scripta Mater. 53 (2005) 585–589.
[21] C.T. Chi, C.G. Chao, T.F. Liu, C.C. Wang, Mater. Sci. Eng. A, submitted for publication.
[22] ASTM B557-02 (2002), pp. 1–15.
[23] F. Czerwinski, Acta Mater. 50 (2002) 2639–2654.
[24] M.H. Zayan, Oxid. Met. 34 (1990) 465–472.
[25] F. Czerwinski, Corros. Sci. 46 (2004) 377–386.
[26] P. Liang, T. Tarfa, J.A. Robinson, S. Wagner, P. Ochin, M.G. Harmelin, H.J. Seifert, H.L. Lukas, F. Aldinger, Thermochim. Acta 314 (1998) 87–110.
[27] E.F. Emley, Principles of Magnesium Technology, Pergamon Press, Oxford, 1966.